An improved numerical scheme for coffee Extraction Yield evaluation

Nadaniela Egidi [a],[*], Josephin Giacomini [a], Elisabeth Larsson [b], Alessia Perticarini [c]

[a] School of Science and Technology - Mathematics Division, University of Camerino, via Madonna delle Carceri 9, Camerino (MC), 62032, Italy
[b] Department of Information Technology, Uppsala University, SE-751 05, Uppsala, Sweden
[c] Dipartimento di Matematica e Applicazioni "Renato Caccioppoli", Università degli Studi di Napoli "Federico II", Naples, Italy

ARTICLE INFO

ABSTRACT

This work proposes a polynomial-augmented radial basis function (RBF) collocation method with polyharmonic to solve the advection–diffusion–reaction (ADR) equations associated with the percolation process for espresso extraction. Numerical methods for solving these equations are useful for many applications where we have chemical reactions and transport in a porous medium. Polynomial augmentation in RBF collocation is useful when it is also necessary to approximate the derivatives, to overcome the stagnation error problem. Moreover, the polyharmonic RBF avoids the hassle of determining the shape parameter. The proposed meshless method allows for discretising the ADR equations and obtaining a numerical solution used to evaluate the efficiency of the extraction process in espresso coffee; this method can be easily generalised to higher dimensions or more complex domains. The numerical results have been compared to measurements carried out in the laboratory.

1. Introduction

Coffee is one of the most popular drinks after milk and tea, and the espresso coffee industry is increasingly attentive to environmental sustainability. A significant problem, in espresso extraction, is to maximise the beverage quality and minimise the raw material. To this aim, the Extraction Yield (EY) is used in the coffee industry to evaluate the efficiency of the extraction process [1]. The EY is equal to the ratio between the mass of solubles extracted and transported into the cup and the mass of coffee powder, hence it is a dimensionless value. The EY can be computed from the Total Dissolved Solids (TDS) divided by the brew ratio. The TDS can be obtained by properly drying a small amount of espresso coffee and weighing the residue made of solids, or by using a refractometer; in fact, the TDS is the ratio between the mass of dissolved substances and the mass of the beverage. Finally, the brew ratio is obtained by dividing the mass of the dry coffee powder used in the preparation by the mass of the liquid beverage. We recall that the Specialty Coffee Association in the brewing chart [1] refers to 18%–22% as the optimal range for the EY; larger values lead to coffee having too bitter and astringent taste (over-extraction); whereas lower ones lead to coffee whose taste is too acidic and sweet (under-extraction). Indicators EY and TDS have been extensively studied: the studies in [2,3] exploit TDS for a comparison between different extraction methods; in [4], the TDS is chosen as an extraction efficiency indicator for different roasting degrees and grinding levels of espresso, American and Turkish brewing; the research in [5–7] exploit TDS and EY to observe the consequences

on the extraction of variation of water pressure, grinding level and temperature gradient on the espresso coffee. Furthermore, [8] uses the TDS to investigate the concentration of chemicals in espresso while decreasing the quantity of coffee powder in three different filter baskets. Although there are many studies on the relationship between these indicators and coffee chemistry, only recently mathematical models have been considered in the coffee extraction. In [9], the EY is computed by a uni-dimensional percolation model. This model is also used in [10] for computing the TDS, moreover, the used numerical scheme guarantees the positivity of the solution and mass conservation. This solving strategy is also used in [11] and the model has been generalised, to deal with multiple chemical species. Like all uni-dimensional models, they are simple but only consider average quantities calculated over the entire domain or parts of it [12]. A more refined three-dimensional model, considering the main percolation processes that occur during the espresso extraction, has been proposed in [13,14].

In this work we propose a simple tool useful for the coffee industry to evaluate the EY. In particular, following the idea in [9,15,16], the percolation model discards the initial imbibition phase and an ADR equation is coupled with a diffusion equation. Initially, each grain is supposed wet, and the equations describe the mass transport and the dissolution of species, occurring during the extraction process. These equations are extensively used for modelling real-life phenomena [17,18], but their analytical solutions are usually unknown

---

* Corresponding author.
E-mail addresses: nadaniela.egidi@unicam.it (N. Egidi), josephin.giacomini@unicam.it (J. Giacomini), elisabeth.larsson@it.uu.se (E. Larsson), alessia.perticarini@unicam.it (A. Perticarini).

because such models are very complex. To compute the numerical solution of such kinds of equations, it is fundamental to use efficient numerical schemes such as those based on upwind finite difference schemes and the Runge–Kutta ones. Lately, various alternatives have been proposed such as the one in [19], where an operator splitting method is used to construct an algorithm to solve both fast and slow reaction problems, that occur during bimolecular reactive processes in porous media. Moreover, [20,21] propose an explicit method that is unconditionally stable and preserves the positivity, while [22] uses a local radial basis function (RBF) method for studying Turing systems and bacterial chemotaxis processes, dealing with domains with a complex shape and large-scale problems. Finally, [23,24] use RBFs together with finite difference to calculate the approximate solution of one and two-dimensional time-fractional stochastic Sine–Gordon equation.

In [10,11], the involved equations are discretised by finite differences. Instead, in this work we use the RBFs in the collocation method for discretising the percolation model. The reason for this choice comes from the fact that the so-called meshless methods operate with nodes rather than meshes. Hence, the proposed discretisation technique does not require grid generation, and its generalisation to two or three-dimensional cases is immediate. Moreover, meshless methods are more appropriate than finite differences or finite element methods, in the case of very large mesh deformation and moving discontinuities. In particular, the polynomial-augmented polyharmonic spline of exponent 3 is the RBF chosen in this article. Thus, the main advantages of the proposed technique are the independence from the mesh and the independence from the shape parameter. The proposed scheme can be easily generalised to greater dimensions, as it is a meshfree method, so it only needs the nodes' information, on the other hand, preconditioning techniques must be used because the ill-conditioning of the RBF interpolation matrix when we have a large number of nodes. In addition, to evaluate the capacity of the proposed scheme in the prediction of the EY, the numerical results have been compared with the EY values measured in the laboratory, and the used samples of espresso coffee have been collected by considering various conditions for the extraction.

The article is organised as follows. Section 2 describes the considered percolation model. In Section 3 the numerical approximation scheme used for the solution of the mathematical model is presented. Section 4 describes the laboratory tests performed for measuring the EY, the numerical results obtained with the proposed method, and a comparison between numerical and measured values. Finally, future developments are discussed in Section 5.

2. The percolation model

The espresso coffee extraction is obtained when the pressurised hot water seeps through the tamped coffee powder contained in the filtering basket. During the percolation process, the chemical substances contained in the coffee powder, that have been previously roasted, are dissolved by the water that seeps through the void spaces between the coffee grains. In detail, at the beginning, in the imbibition phase, the water flowing through the powder, under the only effect of gravity, penetrates the grains by capillarity and dissolves the chemical substances. Subsequently, during the extraction phase, the dissolved materials are transported into the cup by pressurised hot water. The high pressure of the water is necessary to overcome the resistance opposed by the compact porous medium.

We note that the substances, contained in the larger grains, are only partially dissolved and most of the dissolved chemicals come from the smaller grains [12]. Therefore, the mathematical model for the description of the dynamics occurring in the coffee extraction has to be capable of describing the transport of chemicals from the interior of the grains to their external surfaces, their dissolution into the liquid, and the transport process due to the fluid flow through the coffee pod.

In the following, for the reader's convenience, we briefly discuss the adopted model.

Both the solid and the liquid phases, and the main physico-chemical processes are considered during the modelling of the espresso coffee extraction. These are the diffusion and the advective transport of chemicals in the liquid phase, and the only diffusion phenomena of the species within each grain of the solid phase.

Here the coffee powder is approximated through spheres of two distinct radii a^b and a^f, for boulders (coarse grains) and fines (fine grains), respectively. This assumption is because grinding machines produce coffee powder with a bimodality feature of its granulometry, see Section 4.1 for details. The extraction is affected by the dimension of the grains, in particular: i) it affects the porosity of the medium since boulders and fines create the coffee pod, that is the porous medium where the percolation takes place; ii) it affects the dissolution rate of the species, because the sizes of the grains, i.e., their radii, influence the time during which chemicals are subject to diffusive transport in grains. We suppose that the coffee pod is a cylinder of height L and circular base of radius R_0, and that the vertical axis is oriented such that the cylinder has the upper base in $z = 0$ and the lower base in $z = L$.

We know that the water flows predominantly along the vertical axis, so we can describe the coffee extraction by a uni-dimensional model, considering only the vertical direction. On the other hand, the dissolution processes for chemicals in the solid phase occur predominantly along the radial direction, therefore, a uni-dimensional model, along the radial direction for each fixed z-level, can be used to describe the dynamics of the solid phase. In more detail, along the vertical direction, we model the transport and the inter-grain flow, while along the radial direction, we model the intra-grain transport. Let c^f and c^b be the concentration of the chemicals contained in the fine and big grains, respectively. The concentration of substances dissolved and transported by the water is denoted by c^l and is called the liquid phase concentration. Thus, we are assuming a common behaviour for different chemical substances. Note that this simplification is not a problem for our purpose: the calculation of EY. See [11,13] for models dealing with different species.

Let $\tau > 0$ be the percolation time, the dynamics of the concentration $c^l(z, t)$, $z \in (0, L)$, $t \in (0, \tau)$, of chemicals in the liquid phase is described by

$$\begin{cases} (1 - \phi) \dfrac{\partial c^l}{\partial t}(z, t) - D \dfrac{\partial^2 c^l}{\partial z^2}(z, t) + q \dfrac{\partial c^l}{\partial z}(z, t) = b^f G^f(z, t) + b^b G^b(z, t), \\ -D \dfrac{\partial c^l}{\partial z}(0, t) + q c^l(0, t) = 0, \\ -D \dfrac{\partial c^l}{\partial z}(L, t) = 0, \\ c^l(z, 0) = 0, \end{cases}$$

$$(1)$$

where ϕ is the local volume fraction occupied by grains, q is the Darcy flux, and D is the effective diffusivity. In particular, ϕ is given by

$$\phi = \phi^f + \phi^b, \quad \phi^f = b^f \frac{a^f}{3}, \quad \phi^b = b^b \frac{a^b}{3},$$

where b^f and b^b are the so-called Brunauer–Emmett–Teller parameters [25], hence ϕ^f and ϕ^b are the volume fractions associated with fines and boulders, respectively. In (1), in addition to the advective term and the diffusive term, there are also G^f and G^b, which are the reactive terms that connect the dynamics of liquid and solid species and will be described in the following. The boundary condition at the inlet ($z = 0$) corresponds to no flux of solubles across the inlet; the boundary condition at the outlet ($z = L$) corresponds to no diffusive flux at the outlet. A null concentration in the liquid phase is imposed as initial condition.

The dynamics of the concentrations of chemicals in the solid phase, at level $z \in (0, L)$, are modelled by the following initial–boundary value problems for the two different kinds of grains considered $s = f, b$:

$$\begin{cases} \dfrac{\partial c^s}{\partial t}(r, z, t) = \dfrac{D_g}{r^2} \dfrac{\partial}{\partial r}\left(r^2 \dfrac{\partial c^s}{\partial r}(r, z, t)\right), \\[2mm] -D_g \dfrac{\partial c^s}{\partial r}(0, z, t) = 0, \\[2mm] -D_g \dfrac{\partial c^s}{\partial r}(a^s, z, t) = G^s(z, t), \\[2mm] c^s(r, z, 0) = c_0, \end{cases} \qquad (2)$$

where $t \in (0, \tau)$, $r \in (0, a^s)$, c_0 is the initial solid concentration and D_g is the diffusivity and is assumed to be independent of particle size. In particular, we suppose the grains have spherical symmetry, so in problem (2) we have the diffusion equation in spherical coordinates for the transport. We highlight that $c^s = c^s(r, z, t)$, this means that we have one problem of type (1), which for each z-level is coupled with two problems of kind (2), one for the solid concentrations c^f and the other for c^b. The terms G^s give the coupling, modelling the transfer of the chemicals from the grains into the liquid. In particular, for $s = f, b$ we have

$$G^s(z, t) = k_r c^s(a^s, z, t) \max\left(c^s(a^s, z, t) - c^l(z, t), 0\right) \cdot \max\left(c_{\text{sat}} - c^l(z, t), 0\right), \qquad (3)$$

where k_r is the reaction rate, c_{sat} is the concentration at saturation of the liquid, and $\max(x, 0)$ is the continuous, non-differentiable function that selects the maximum non-negative argument. Because of the high non-linearity of Formula (3), particular attention is necessary for its solution, see [9–11,26] for a wide discussion. The coupled problems (1) and (2) determine the complete mathematical model for the unknown concentrations c^l, c^f, c^b. From the solutions of problem (1)–(2) we obtain the EY using the following formula

$$EY = \frac{q}{\phi^s \rho L} \int_0^\tau c^l(L, t) dt, \qquad (4)$$

where ρ denotes the coffee grain density, see [10] for a detailed derivation of this formula.

3. Numerical approximation

In this section, we illustrate the used approximation scheme for problem (1)–(2). In particular, the spatial derivatives are approximated via RBFs. In more detail, in Section 3.1 we present the RBF approximation and introduce the matrix notation that will be useful in the following section. Then, in Section 3.2 we describe the numerical scheme adopted in the discretisation of problem (1)–(2).

3.1. Matrix form of the RBFs interpolation system

RBFs are powerful tools in the approximation of functions, including solutions of partial differential equations. Let $\varphi : \mathbb{R}^+ \to \mathbb{R}$ be an RBF and let $x_j \in \mathbb{R}^d$, $j = 1, 2, \ldots, n$, be scattered nodes, then we can approximate the function $f : \Omega \subset \mathbb{R}^d \to \mathbb{R}$ at the point $x \in \Omega$ with

$$\tilde{f}(x) = \sum_{j=1}^n \lambda_j \varphi\left(\|x - x_j\|\right) \equiv \sum_{j=1}^n \lambda_j \varphi_j(x), \qquad (5)$$

where λ_j are unknown coefficients which can be determined by imposing the interpolation conditions $\tilde{f}(x_i) = f(x_i)$, $i = 1, 2, \ldots, n$. This leads to the following linear system

$$\underbrace{\begin{pmatrix} \varphi_1(x_1) & \cdots & \varphi_n(x_1) \\ \vdots & & \vdots \\ \varphi_1(x_n) & \cdots & \varphi_n(x_n) \end{pmatrix}}_{A} \underbrace{\begin{pmatrix} \lambda_1 \\ \vdots \\ \lambda_n \end{pmatrix}}_{\lambda} = \underbrace{\begin{pmatrix} f(x_1) \\ \vdots \\ f(x_n) \end{pmatrix}}_{f}, \qquad (6)$$

whose solution is:

$$\lambda = A^{-1} f. \qquad (7)$$

Note that, for positive definite RBFs the matrix A is guaranteed to be non-singular for distinct node points [27]. In the following, we refer to A as the RBF interpolation matrix associated with the interpolation nodes x_j, $j = 1, 2, \ldots, n$.

Therefore, if $\mathcal{L}$ is a linear operator, then from Eq. (5) we have

$$\begin{aligned} \mathcal{L}\tilde{f}(x) &= \sum_{j=1}^n \lambda_j \mathcal{L}\varphi_j(x) = \underbrace{\left(\mathcal{L}\varphi_1(x), \ldots, \mathcal{L}\varphi_n(x)\right)}_{a(x)^{\mathcal{L}}} \lambda = \\ &= a(x)^{\mathcal{L}} A^{-1} f, \end{aligned} \qquad (8)$$

where, in the last equality, we exploited equation (7). Let $p \in \mathbb{N}$, $m = \begin{pmatrix} p + d \\ d \end{pmatrix}$, $\mathcal{B} = \{p_j(x) : j = 1, 2, \ldots, m\}$ be a basis of the space of polynomials in $x \in \mathbb{R}^d$, with real coefficients, of degree at most p. We note that m is the dimension of the polynomial space. In addition, we require that the discretised basis $\mathcal{B}$ is orthogonal to the RBF coefficients λ, that is:

$$\sum_{j=1}^n \lambda_j p_k(x_j) = 0, \ k = 1, 2, \ldots, m. \qquad (9)$$

Then, we can consider the following approximation of f:

$$\hat{f}(x) = \sum_{j=1}^n \lambda_j \varphi_j(x) + \sum_{j=1}^m \mu_j p_j(x). \qquad (10)$$

As before, if we denote with $P_{ij} = p_j(x_i)$ and $\mu = (\mu_1, \mu_2, \ldots, \mu_m)^T$, imposing the interpolation conditions $\hat{f}(x_i) = f(x_i)$, $i = 1, 2, \ldots, n$, and the orthogonality conditions (9), we obtain:

$$\underbrace{\begin{pmatrix} A & P \\ P^T & 0 \end{pmatrix}}_{\hat{A}} \begin{pmatrix} \lambda \\ \mu \end{pmatrix} = \begin{pmatrix} f \\ 0 \end{pmatrix}, \qquad (11)$$

whose solution is

$$\begin{pmatrix} \lambda \\ \mu \end{pmatrix} = \hat{A}^{-1} \begin{pmatrix} f \\ 0 \end{pmatrix}. \qquad (12)$$

However, we have to require that P has full rank. This is a condition on the nodes to be unisolvent for polynomials of degree p, which is always true in $\mathbb{R}$ for distinct points. Under this condition, the invertibility of $\hat{A}$ is guaranteed as shown in [28,29]. In the following, we refer to $\hat{A}$ as the polynomially augmented RBF (PA-RBF) interpolation matrix associated with the interpolation nodes x_j, $j = 1, 2, \ldots, n$.

Thus, applying the operator $\mathcal{L}$ to $\hat{f}$, exploiting relation (12) and using the following notation

$$p(x)^{\mathcal{L}} = (\mathcal{L}p_1(x), \ldots, \mathcal{L}p_m(x)),$$

we obtain:

$$\begin{aligned} \mathcal{L}\hat{f}(x) &= \underbrace{\left(a(x)^{\mathcal{L}} \quad p(x)^{\mathcal{L}} \right)}_{b(x)^{\mathcal{L}}} \begin{pmatrix} \lambda \\ \mu \end{pmatrix} = \\ &= b(x)^{\mathcal{L}} \hat{A}^{-1} \begin{pmatrix} f \\ 0 \end{pmatrix} = (b(x)^{\mathcal{L}} \hat{A}^{-1})_{1:n} f, \end{aligned} \qquad (13)$$

where the notation $(\cdot)_{1:n}$ denotes the first n components of the vector $(\cdot)$. Therefore, Eqs. (8) and (13) allow us to approximate the action of the operator $\mathcal{L}$ on the function f in the point x as a linear combination of the values of f in the nodal points.

3.2. Numerical scheme

Let $\mathcal{Z} = \{z_j\}_{j=0,1,\ldots,N} \subseteq [0, L]$ be a set of distinct discretisation nodes along the vertical direction, such that $z_0 = 0$ and $z_N = L$. Let z_{-1} be a node in a left neighbourhood of 0 and z_{N+1} be a node in a right
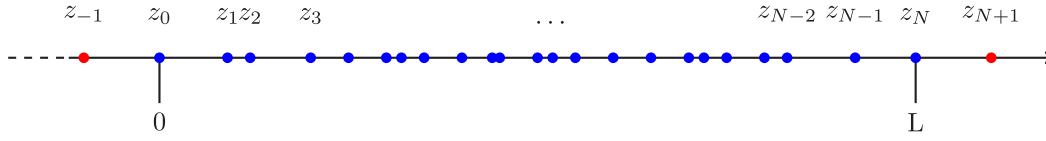
Fig. 1. Graphical representation of points in $\bar{\mathcal{Z}}$.

neighbourhood of L, we choose $\bar{\mathcal{Z}} = \mathcal{Z} \cup \{z_{-1}, z_{N+1}\}$ as the set of the interpolation nodes. In Fig. 1, we show the points of $\mathcal{Z}$ in blue, and the points of $\bar{\mathcal{Z}} \setminus \mathcal{Z}$ in red.

Similarly, for $s = b, f$, let $\mathcal{R}^s = \{r_k^s\}_{k=0,1,\ldots,M^s} \subseteq [0, a^s]$ be a set of distinct discretisation nodes along the radial direction in fines and boulders, we use $\bar{\mathcal{R}}^s = \mathcal{R}^s \cup \{r_{-1}^s, r_{M^s+1}^s\}$ as the set of interpolation nodes in the radial direction, where r_{-1}^s is a point in a left neighbourhood of 0 and $r_{M^s+1}^s$ in a right neighbourhood of a^s.

Let Z and R^s, $s = f, b$, be the PA-RBF interpolation matrices associated with the interpolation nodes $\bar{\mathcal{Z}}$ and $\bar{\mathcal{R}}^s$, respectively. We note that these matrices satisfy equations of the form (11) and $d = 1$. Thus, for a fixed time t, if we collect in the vector $\boldsymbol{c}^l(t)$ the values of the liquid concentration $c^l(z, t)$ calculated at the points of $\bar{\mathcal{Z}}$, that is $\boldsymbol{c}^l(t) = \left(c^l(z_j, t)\right)_{j=-1,0,\ldots,N+1}$, the analogue of Eq. (13) for the liquid concentration c^l, is:

$$\mathcal{L}\hat{c}^l(z, t) = \left(\boldsymbol{b}(z)^{\mathcal{L}} Z^{-1}\right)_{-1:N+1} \boldsymbol{c}^l(t). \tag{14}$$

Similarly, for fixed t and z, if we collect the values of the solid concentrations $c^s(r, z, t)$, $s = f, b$, calculated at the points of $\bar{\mathcal{R}}^s$ in the vectors $\boldsymbol{c}^s(z, t)$, that is $\boldsymbol{c}^s(z, t) = \left(c^s(r_k^s, z, t)\right)_{k=-1,0,\ldots,M^s+1}$, the analogue of Eq. (13) for the solid concentrations c^s are

$$\mathcal{L}\hat{c}^s(r, z, t) = \left(\boldsymbol{b}(r)^{\mathcal{L}} (R^s)^{-1}\right)_{-1:M^s+1} \boldsymbol{c}^s(z, t). \tag{15}$$

We denote with $\mathcal{L}_0$ the identity operator and with $\mathcal{L}_1$ and $\mathcal{L}_2$ the first and second derivative operators respect to z, respectively. For each of these operators, we can impose equation (14) at each point of $\mathcal{Z}$. For instance, for the first derivative, this leads to:

$$\left(\mathcal{L}_1 \hat{c}^l(z_j, t)\right)_{j=0,1,\ldots,N} = \left(Z_z Z^{-1}\right)_{:,-1:N+1} \boldsymbol{c}^l(t) \equiv Z^z \boldsymbol{c}^l(t), \tag{16}$$

where $Z_z \equiv \left(\boldsymbol{b}(z_j)^{\mathcal{L}_1}\right)_{j=0,1,\ldots,N}$ has $N + 1$ rows, moreover, $Z^z = \left(Z_z Z^{-1}\right)_{:,-1:N+1}$ is called differentiation matrix of first order. Similarly, for $\mathcal{L}_0$ and $\mathcal{L}_2$ with matrices Z_0 and Z_{zz}, respectively.

Similarly, for fixed z_j we can impose equation (15) in each point of $\mathcal{R}^s$. For the second order differential operator respect to r, that with an abuse of notation we denote with $\mathcal{L}_2$, this leads to:

$$\begin{aligned}\left(\mathcal{L}_2 \hat{c}^s(r_k^s, z_j, t)\right)_{k=0,1,\ldots,M^s} = \\ = \left(R_{rr}^s (R^s)^{-1}\right)_{:,-1:M^s+1} \boldsymbol{c}^s(z_j, t) \equiv R^{s,rr} \boldsymbol{c}^s(z_j, t),\end{aligned} \tag{17}$$

where $R_{rr}^s \equiv \left(\boldsymbol{b}(r_k^s)^{\mathcal{L}_2}\right)_{k=0,1,\ldots,M^s}$, $s = f, b$, defines the differentiation matrices of second order in the radial direction $R^{s,rr}$. Similarly, for $\mathcal{L}_0$ and $\mathcal{L}_1$ with matrices R_0^s and R_r^s, respectively, for $s = f, b$.

In more detail, we have:

$$I^z = \left(Z_0 Z^{-1}\right)_{:,-1:N+1},$$
$$Z^z = \left(Z_z Z^{-1}\right)_{:,-1:N+1},$$
$$Z^{zz} = \left(Z_{zz} Z^{-1}\right)_{:,-1:N+1},$$
$$I^s = \left(R_0^s (R^s)^{-1}\right)_{:,-1:M^s+1}, \qquad s = f, b,$$
$$R^{s,r} = \left(R_r^s (R^s)^{-1}\right)_{:,-1:M^s+1}, \qquad s = f, b,$$
$$R^{s,rr} = \left(R_{rr}^s (R^s)^{-1}\right)_{:,-1:M^s+1}, \qquad s = f, b.$$

We define some useful notations for the systems below. A matrix endowed with the subscript j denotes the single jth row of the corresponding original matrix (i.e., the matrix without the subscript j). This means that, regardless of the vertical or radial coordinate, the subscript 0 denotes the first row of the matrix that corresponds to the point $z_0 = 0$ or $r_0^s = 0$, $s = f, b$, respectively. Similarly, the subscripts

N and M^s, $s = f, b$ denote the row of the matrix corresponding to the boundary points $z_N = L$ and $r_{M^s}^s = a^s$, $s = f, b$, respectively. Moreover, in the following solid systems, we use this notation: a matrix equipped with the subscript I is the sub-matrix that consists of all the rows of the corresponding original matrix except the ones corresponding to the left boundary point, $z_0 = 0$ or $r_0^s = 0$, $s = f, b$, that is for instance: $R_I^{s,r} = (R^{s,r})_{1:M^s,:}$.

With the above described notations, we can express the liquid phase system as:

$$\begin{cases} (1 - \phi) I^z \dfrac{\partial \boldsymbol{c}^l(t)}{\partial t} = D Z^{zz} \boldsymbol{c}^l(t) - q Z^z \boldsymbol{c}^l(t) + \\ \qquad\qquad + b^f \boldsymbol{G}^f(t) + b^b \boldsymbol{G}^b(t), \\ -D Z_0^z \boldsymbol{c}^l(t) + q I_0^z \boldsymbol{c}^l(t) = 0, \\ -D Z_N^z \boldsymbol{c}^l(t) = 0, \\ \boldsymbol{c}^l(0) = 0, \end{cases} \tag{18}$$

where for each vertical level z_j, $j = 0, 1, \ldots, N$, we collect the reactive terms into vectors $\boldsymbol{G}^s(t)$, $s = f, b$, whose components are given by

$$G^s(z_j, t) = k_r I_{M^s}^s \boldsymbol{c}^s(z_j, t) \max\left(I_{M^s}^s \boldsymbol{c}^s(z_j, t) - I_j^z \boldsymbol{c}^l(t), 0\right) \cdot \max\left(c_{\text{sat}} - I_j^z \boldsymbol{c}^l(t), 0\right).$$

For each vertical level z_j, $j = 0, 1, \ldots, N$, there are two problems of kind (2) for the solution of the solid phase, coupled to the liquid phase through the non-linear source terms. For $s = f, b$, they are given by:

$$\begin{cases} I_I^s \dfrac{\partial \boldsymbol{c}^s(z_j, t)}{\partial t} = D_g \left(\dfrac{2}{r} R_I^{s,r} \boldsymbol{c}^s(z_j, t) + R_I^{s,rr} \boldsymbol{c}^s(z_j, t)\right), \\ I_0^s \dfrac{\partial \boldsymbol{c}^s}{\partial t}(z_j, t) = 3 D_g R_0^{s,rr} \boldsymbol{c}^s(z_j, t), \\ -D_g R_0^{s,r} \boldsymbol{c}^s(z_j, t) = 0, \\ -D_g R_{M^s}^{s,r} \boldsymbol{c}^s(z_j, t) = G^s(z_j, t), \\ \boldsymbol{c}^s(z_j, 0) = c_0. \end{cases} \tag{19}$$

We note that at $r = 0$, the following discretisation based on De L'Hôpital rule has been used

$$\begin{aligned} \frac{\partial c^s}{\partial t}(0, z, t) &= \lim_{r \to 0} \left(\frac{2}{r} D_g \frac{\partial c^s}{\partial r}(r, z, t) + D_g \frac{\partial^2 c^s}{\partial r^2}(r, z, t)\right) = \\ &= 3 D_g \frac{\partial^2 c^s}{\partial r^2}(0, z, t). \end{aligned}$$

Now we can apply the time discretisation to problems (18), (19) and use a method resembling the Crank–Nicolson method for both linear and non-linear parts while the boundary conditions are implemented at the new time level. Note that we use the time index as a superscript to indicate a discrete time level.

We start with the time discretisation of the PDE for the liquid phase, as a help to see how we will reorder it. Let N_t be a positive integer such that $h_t = \tau / N_t$, for $n = 0, 1, \ldots, N_t - 1$ we have:

$$\begin{aligned} (1 - \phi) I^z (\boldsymbol{c}^{l,n+1} - \boldsymbol{c}^{l,n}) = \frac{h_t}{2} \big(D Z^{zz} \boldsymbol{c}^{l,n+1} - q Z^z \boldsymbol{c}^{l,n+1} + \\ + b^f \boldsymbol{G}^{f,n+1} + b^b \boldsymbol{G}^{b,n+1} + D Z^{zz} \boldsymbol{c}^{l,n} + \\ - q Z^z \boldsymbol{c}^{l,n} + b^f \boldsymbol{G}^{f,n} + b^b \boldsymbol{G}^{b,n} \big), \end{aligned}$$

where $\boldsymbol{c}^{l,n} \approx \boldsymbol{c}^l(t_n)$, $n = 0, 1, \ldots, N_t$. Thus, we get:

$$
\begin{cases}
\left[(1-\phi) I^z - \dfrac{h_t}{2} (DZ^{zz} - qZ^z)\right] \boldsymbol{c}^{l,n+1} = \\
\quad = \left[(1-\phi) I^z + \dfrac{h_t}{2} (DZ^{zz} - qZ^z)\right] \boldsymbol{c}^{l,n} + \\
\quad + \dfrac{h_t}{2} \left(b^f \boldsymbol{G}^{f,n+1} + b^b \boldsymbol{G}^{b,n+1} + b^f \boldsymbol{G}^{f,n} + b^b \boldsymbol{G}^{b,n} \right), \\
-DZ_0^z \boldsymbol{c}^{l,n+1} + q I_0^z \boldsymbol{c}^{l,n+1} = 0, \\
-DZ_N^z \boldsymbol{c}^{l,n+1} = 0, \\
\boldsymbol{c}^{l,0} = 0.
\end{cases}
\tag{20}
$$

We do the same for the solid phases and, for $s = f, b$, we obtain

$$
I_I^s \left(\boldsymbol{c}^{s,n+1}(z_j) - \boldsymbol{c}^{s,n}(z_j) \right) = \frac{h_t}{2} D_g \left(\frac{2}{r} R_I^{s,r} \boldsymbol{c}^{s,n+1}(z_j) + \right.
$$
$$
\left. + R_I^{s,rr} \boldsymbol{c}^{s,n+1}(z_j) + \frac{2}{r} R_I^{s,r} \boldsymbol{c}^{s,n}(z_j) + R_I^{s,rr} \boldsymbol{c}^{s,n}(z_j) \right),
$$

where $\boldsymbol{c}^{s,n}(z_j) \approx \boldsymbol{c}^s(z_j, t_n)$, $j = -1, 0, \ldots, N+1$, $n = 0, 1, \ldots, N_t$. The corresponding systems are

$$
\begin{cases}
\left[I_I^s - \dfrac{D_g h_t}{2} \left(\dfrac{2}{r} R_I^{s,r} + R_I^{s,rr} \right)\right] \boldsymbol{c}^{s,n+1}(z_j) = \\
\quad = \left[I_I^s + \dfrac{D_g h_t}{2} \left(\dfrac{2}{r} R_I^{s,r} + R_I^{s,rr} \right)\right] \boldsymbol{c}^{s,n}(z_j), \\
\left[I_0^s - \dfrac{3 D_g h_t}{2} R_0^{s,rr}\right] \boldsymbol{c}^{s,n+1}(z_j) = \\
\quad = \left[I_0^s + \dfrac{3 D_g h_t}{2} R_0^{s,rr}\right] \boldsymbol{c}^{s,n}(z_j), \\
-D_g R_0^{s,r} \boldsymbol{c}^{s,n+1}(z_j) = 0, \\
-D_g R_{M^s}^{s,r} \boldsymbol{c}^{s,n+1}(z_j) = G^{s,n+1}(z_j), \\
\boldsymbol{c}^{s,0}(z_j) = c_0,
\end{cases}
\tag{21}
$$

In systems (21), the concentrations $\boldsymbol{c}^{s,n}(z_j)$, $s = f, b$ depend on z_j, therefore such systems must be solved for each vertical level z_j. Moreover, systems (20), (21) are coupled through the reactive terms G^s, whose approximations $G^{s,n}(z_j)$, $s = f, b$, are obtained from

$$
G^{s,n}(z_j) = k_r I_{M^s}^s \boldsymbol{c}^{s,n}(z_j) f_\alpha \left(I_{M^s}^s \boldsymbol{c}^{s,n}(z_j) - I_j^z \boldsymbol{c}^{l,n} \right) \cdot
$$
$$
\cdot f_\alpha \left(c_{\text{sat}} - I_j^z \boldsymbol{c}^{l,n} \right),
$$

$$
f_\alpha(x) = \begin{cases} \exp\left(\dfrac{x}{\alpha} + \log(\alpha) - 1 \right), & x \le \alpha \\ x, & x > \alpha, \end{cases}
\tag{22}
$$

with $\alpha > 0$. The parameter α must be chosen sufficiently small in such a way that f_α is an approximation of the function $\max(x, 0)$. We note that f_α is continuous and differentiable and the system can be written as

$$
A\sigma^{n+1} = C\sigma^n + \varphi^{n+1}, \qquad n = 0, \ldots, N_t - 1,
\tag{23}
$$
$$
B\lambda^{n+1} = E\lambda^n + \psi^{n+1} + \psi^n, \ n = 0, \ldots, N_t - 1,
\tag{24}
$$

where

$A, C \in \mathbb{R}^{(N+1)(M^f+M^b+6) \times (N+3)(M^f+M^b+6)}$,

$B, E \in \mathbb{R}^{(N+3) \times (N+3)}$,

$\sigma^n \in \mathbb{R}^{(N+1)(M^f+M^b+6)}$, $\lambda^n \in \mathbb{R}^{N+3}$, $n = 0, \ldots, N_t - 1$,

$\varphi^n \in \mathbb{R}^{(N+1)(M^f+M^b+6)}$, $\psi^n \in \mathbb{R}^{N+3}$, $n = 0, \ldots, N_t - 1$.

The vectors σ^n and λ^n are defined as

$$
\sigma^n = \begin{pmatrix} \mathbf{c}^{f,n} \\ \mathbf{c}^{b,n} \end{pmatrix},
$$
$$
\lambda^n = \left(c_{-1}^{l,n}, c_0^{l,n}, \ldots, c_{N+1}^{l,n} \right)^T,
\tag{25}
$$

with

$$
\mathbf{c}^{f,n} = \left(c_{-1}^{f,n}(z_0), c_0^{f,n}(z_0), \ldots, c_{M^f+1}^{f,n}(z_0), \right.
$$
$$
c_{-1}^{f,n}(z_1), c_0^{f,n}(z_1), \ldots, c_{M^f+1}^{f,n}(z_1), \ldots,
$$
$$
\left. \ldots, c_{-1}^{f,n}(z_N), c_0^{f,n}(z_N), \ldots, c_{M^f+1}^{f,n}(z_N) \right)^T,
$$

and analogously for the vector $\mathbf{c}^{b,n}$. In particular σ^n and λ^n are unknown for $n \ge 1$, instead λ^0 is the null vector and, for $s = f, c$, $\boldsymbol{c}^{s,0}$ are the vectors having all entries equal to c_0. The non-linear terms are in

$$
\varphi^n = \begin{pmatrix} \mathbf{F}^{f,n} \\ \mathbf{F}^{b,n} \end{pmatrix},
$$
$$
\psi^n = \left(0, \frac{h_t}{2} b^f G^{f,n}(z_0) + \frac{h_t}{2} b^b G^{b,n}(z_0), \ldots, \frac{h_t}{2} b^f G^{f,n}(z_N) + \frac{h_t}{2} b^b G^{b,n}(z_N), 0 \right)^T,
$$
$$
\mathbf{F}^{s,n} = \left(0, \ldots, 0, G^{s,n}(z_0), 0, \ldots, 0, \ldots, 0, G^{s,n}(z_N), 0 \right)^T,
$$

The vector $\mathbf{F}^{s,n}$ has zero components outside the positions $M^s + 2 + k(M^s + 3)$, $k = 0, \ldots, N$. Thus, for the solution of system (23), (24) we apply the nested fixed-point iteration procedure. We note that the solid global matrices A and C are not strictly necessary for the procedure, we can solve the two solids systems consecutively; however, we defined these matrices for the reader's convenience, since they are useful in Algorithm 1, where we give the solving strategy.

Algorithm 1: Given c_0, $maxit_1$, $maxit_2$, tol_1 and tol_2 compute the solution σ^n, λ^n, $n = 1, \ldots, N_t$, of system (23),(24), by the following steps.

1 $\sigma^0 = (c_0, \ldots, c_0)^T$; $\lambda^0 = (0, \ldots, 0)^T$;
2 **for** $n = 0, 1, \ldots, N_t - 1$ **do**
3 $\quad$ $\bar{v} = \tilde{v} = 1$;
4 $\quad$ $\sigma_{1,\bar{v}}^{n+1} = \sigma^n$; $\lambda_{1,\bar{v}}^{n+1} = \lambda^n$;
5 $\quad$ **for** $\mu = 2, 3, \ldots, maxit_2$ **do**
6 $\quad\quad$ $\sigma_{\mu,1}^{n+1} = \sigma_{\mu-1,\tilde{v}}^{n+1}$;
7 $\quad\quad$ **for** $v = 2, 3, \ldots, maxit_1$ **do**
8 $\quad\quad\quad$ $\lambda_{\mu,v-1}^{n+1} = \lambda_{\mu-1,\tilde{v}}^{n+1}$;
9 $\quad\quad\quad$ Compute $\sigma_{\mu,v}^{n+1}$ from $A\sigma_{\mu,v}^{n+1} = C\sigma^n + \varphi_{\mu,v-1}^{n+1}$;
10 $\quad\quad\quad$ **if** $\max\left(\left| \sigma_{\mu,v}^{n+1} - \sigma_{\mu,v-1}^{n+1} \right| \right) \le tol_1$ **then**
11 $\quad\quad\quad\quad$ $\sigma_{\mu,\bar{v}}^{n+1} = \sigma_{\mu,v}^{n+1}$;
12 $\quad\quad\quad\quad$ **break**;
13 $\quad\quad\quad$ **end**
14 $\quad\quad$ **end**
15 $\quad\quad$ $\lambda_{\mu,1}^{n+1} = \lambda_{\mu-1,\tilde{v}}^{n+1}$;
16 $\quad\quad$ **for** $v = 2, \ldots, maxit_1$ **do**
17 $\quad\quad\quad$ $\sigma_{\mu,v-1}^{n+1} = \sigma_{\mu,\bar{v}}^{n+1}$;
18 $\quad\quad\quad$ Compute $\lambda_{\mu,v}^{n+1}$ from $B\lambda_{\mu,v}^{n+1} = E\lambda^n + \psi_{\mu,v-1}^{n+1} + \psi^n$;
19 $\quad\quad\quad$ **if** $\max\left(\left| \lambda_{\mu,v}^{n+1} - \lambda_{\mu,v-1}^{n+1} \right| \right) \le tol_1$ **then**
20 $\quad\quad\quad\quad$ $\lambda_{\mu,\bar{v}}^{n+1} = \lambda_{\mu,v}^{n+1}$;
21 $\quad\quad\quad\quad$ **break**;
22 $\quad\quad\quad$ **end**
23 $\quad\quad$ **end**
24 $\quad\quad$ **if** $\max\left(\left| \sigma_{\mu,\bar{v}}^{n+1} - \sigma_{\mu-1,\tilde{v}}^{n+1} \right| \right) \le tol_2$ *and*
$\quad\quad\quad$ $\max\left(\left| \lambda_{\mu,\bar{v}}^{n+1} - \lambda_{\mu-1,\tilde{v}}^{n+1} \right| \right) \le tol_2$ **then**
25 $\quad\quad\quad$ $\sigma_{\bar{\mu},\bar{v}}^{n+1} = \sigma_{\mu,\bar{v}}^{n+1}$; $\lambda_{\bar{\mu},\bar{v}}^{n+1} = \lambda_{\mu,\bar{v}}^{n+1}$;
26 $\quad\quad\quad$ **break**;
27 $\quad\quad$ **end**
28 $\quad$ **end**
29 $\quad$ $\sigma^{n+1} = \sigma_{\bar{\mu},\bar{v}}^{n+1}$; $\lambda^{n+1} = \lambda_{\bar{\mu},\bar{v}}^{n+1}$
30 **end**

More in detail, for each time step $n = 0, \ldots, N_t - 1$, we consider the following nested fixed-point iteration

$$A\boldsymbol{\sigma}_{\mu,\nu}^{n+1} = C\boldsymbol{\sigma}^n + \boldsymbol{\varphi}_{\mu,\nu-1}^{n+1}, \tag{26}$$

$$B\boldsymbol{\lambda}_{\mu,\nu}^{n+1} = E\boldsymbol{\lambda}^n + \boldsymbol{\psi}_{\mu,\nu-1}^{n+1} + \boldsymbol{\psi}^n, \tag{27}$$

where at time step $n + 1$ we use indices μ and ν for the outer and inner, respectively, fixed-point iteration, and we fix $maxit_1$ and $maxit_2$ such that $\nu \leq maxit_1$ and $\mu \leq maxit_2$. For example, let $\bar{\nu} = \bar{\nu}(\mu)$ be the final inner iteration, then system (26) gives $\boldsymbol{\sigma}_{\mu,\bar{\nu}}^{n+1}$ while system (27) gives $\lambda_{\mu,\bar{\nu}}^{n+1}$. The used stopping criteria for ν and μ depends on a given tolerance $tol_1 > 0$ and is detailed in Algorithm 1, where, for $\boldsymbol{x} \in \mathbb{R}^N$, $\max(\boldsymbol{x})$ is the maximum component of $\boldsymbol{x}$, while $|\boldsymbol{x}|$ is a vector having components equal to the absolute value of the components of $\boldsymbol{x}$. We note that the inner cycle does not take into account the coupling between the two systems. Hence, for refining the results of the inner cycle, we use the outer cycle. In more detail, the final solution of the outer iteration $(\boldsymbol{\sigma}_{\bar{\mu},\bar{\nu}}^{n+1}, \lambda_{\bar{\mu},\bar{\nu}}^{n+1})$ approximates the solution of (23), (24), satisfying the stopping criterium at line 24 in Algorithm 1, where $tol_2 > 0$ denotes a given tolerance. Finally, we used proper parameters ω_l and ω_s, $s = f, b$, in relaxed iterations used to improve the convergence of the inner cycle and help to satisfy the positivity of the solution at the initial time steps. Indeed, without relaxed iteration we observed that the liquid concentration becomes immediately negative instead the solid concentration becomes immediately higher than the initial concentration.

4. Experimental results

In this section, we present both the results obtained from a laboratory extraction campaign and in-silico simulations. The experimental extraction campaign has been described in [10], however, for the reader's convenience we briefly discuss it in Section 4.1, while in Section 4.2 we illustrate the numerical results obtained with the proposed method. We also make a comparison between the laboratory and computational results in terms of the EY.

4.1. Laboratory measurements

The laboratory results are obtained by using the espresso coffee machine Victoria Arduino VA388 Black Eagle [30] for the coffee extraction. The used coffee powder is the pure Arabica coffee Modœtia ground by Mythos 1 [31] and tamped by PUQ® PRESS M2 [32]. All the tools, used during the experimental campaign, were supplied by the company Simonelli Group SpA (Belforte del Chienti, Italy). The extraction procedure applied in the collection of coffee samples is as follows: the VST© Competition filter basket, having an inner radius of 29.25 mm and a height of 26 mm, was filled with 20 ± 0.1 g of powder, which was tamped with a 20 kgF constant tamping force. The extracted coffee mass has been kept at 40 ± 2 g, in this way, we obtained 1:2 as the brew ratio between powder and extracted coffee. The samples were obtained by considering different grain sizes, pressures, and water temperatures. At each extraction, the coffee was collected into a ceramic cup, stirred and cooled down, finally a small amount was inserted in a digital refractometer and the corresponding TDS was measured. For each extraction, the EY was evaluated by the following formula

$$\text{EY} = \frac{\text{TDS}}{\text{brew ratio}}.$$

For the laboratory results, used in the following for the comparison with the computed results, we considered the Modœtia coffee, a water pressure $p = 6, 9$ bar, a water temperature $T = 90.4, 93.4$ °C and a granulometry: optimal, fine, coarse. Where the granulometry is considered optimal when it produces about 40 g of coffee in 25 s at 9 bar and 93.4 °C. Taking this granulometry as a reference, the fine granulometry is obtained by reducing the distance between the burrs of the grinder,

Table 1
For the different granulometry: the mean extraction time τ and the mean height of the tamped powder L.

Coffee type	Optimal		Fine		Coarse	
	L [mm]	τ [s]	L [mm]	τ [s]	L [mm]	τ [s]
Modœtia	13.00	26	13.27	40	14.20	20

Table 2
Laboratory results for TDS measurements, with their standard deviation (σ), and EY, for Modœtia coffee.

T [°C]	p [bar]	τ [s]	Granulometry	TDS [%] (σ)	EY [%]
93.4	9	26	Optimal	10.4 (0.28)	**20.87**
93.4	6	26	Optimal	10.0 (0.12)	**20.43**
90.4	9	26	Optimal	10.2 (0.06)	20.81
90.4	6	25	Optimal	10.2 (0.06)	20.53
93.4	9	39	Fine	10.9 (0.23)	22.09
93.4	6	39	Fine	10.8 (0.25)	22.07
90.4	9	42	Fine	11.0 (0.3)	22.18
90.4	6	41	Fine	11.2 (0.26)	**22.58**
93.4	9	18	Coarse	9.6 (0.50)	19.44
93.4	6	22	Coarse	9.7 (0.31)	**20.11**
90.4	9	19	Coarse	9.5 (0.06)	**19.09**
90.4	6	22	Coarse	10.0 (0.29)	20.10

whereas the coarse is obtained by increasing the distance between the burrs.

For each configuration, we considered three samples obtaining 36 different samples. Obviously, since the brew ratio was kept constant, depending on the granulometry, we obtained different extraction times. Table 1 reports, for different granulometry, the mean height L of the tamped powder and the means τ, of the extraction times, obtained by varying the temperature and the pressure of the water. Moreover, the laser diffraction granulometer Mastersizer 3000, Malvern Instruments [33] has been used for analysing the coffee powder. The particle size distribution curves of the optimal, fine and coarse granulometry profiles of Modœtia coffee powder are shown in Fig. 2. The value on the x-axis is the diameter of the coffee particles, and the percentage of the particles is on the y-axis. From the figure, we can see that all the curves have a local minimum near 100 μm and a bimodal trend. This justifies the choice of considering two families of particles: the fines (diameter ≤ 100 μm) and the boulders (diameter ≥ 100 μm). In the model, this choice is made by assigning the radii for boulders and fines, i.e. a^b and a^f, respectively.

The values of TDS and EY are reported in Table 2, in particular, the minimum value and the maximum value of the EY are reported in bold. From this table, we can see that, for Modœtia, the EY is maximised for fine granulometry, $p = 6$ bar and $T = 90.4$ °C. Hence, the fine granulometry reasonably yields the maximum EY.

4.2. Numerical results

The numerical results are obtained on a PC equipped with an Intel(R) Core(TM) i7-10510U CPU @ 1.80 GHz 2.30 GHz, operative system Windows 11, by implementing in MATLAB R2020a, 64-bit the Algorithm 1, which is a numerical scheme for solving problem (1)–(2)

We use the following physico-chemical parameters, for details on this choice see [9,10,12]: the total solid fraction is $\phi = 0.8272$, the initial solid concentration is $c_0 = 200$ kg/m^3, the concentration of saturation is $c_{sat} = 212.4$ kg/m^3, the liquid diffusivity is $D = 1.0 \cdot 10^{-8}$ m^2/s, the solid diffusivity is $D_g = 6.25 \cdot 10^{-10}$ m^2/s, the reaction rate is $k_r = 6.0 \cdot 10^{-9}$ m^7/kg^2.

In the discretisation scheme, the points in $\mathcal{Z}$ are distributed as half of a Chebyshev nodes set in such a way that we have more points near $z = 0$. We have chosen this distribution for the nodes in $\mathcal{Z}$, since we observed that near $z = 0$ the solution has a steep trend. Instead, the
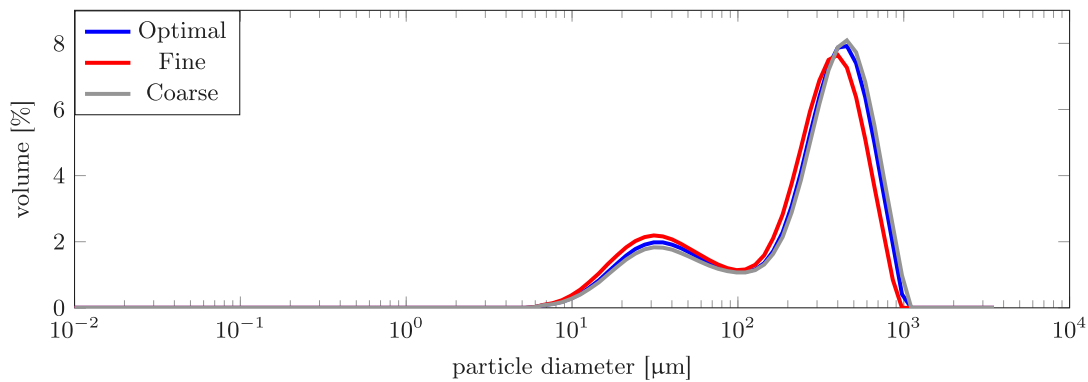
Fig. 2. Distributions of the particles sizes for the Modœtia coffee.

Table 3
Geometrical and physical parameters used in the numerical experiments.

Sample	a^f [μm]	a^b [μm]	ϕ^f	q [10^{-4} m/s]	τ [s]
Fine	15.5	200.0	0.24	3	40
Optimal	16.6	227.0	0.22	4.5	26
Coarse	15.6	227.0	0.20	5.3	20

Table 4
Numerical results of the EY with the corresponding EY ranges from the laboratory experiments.

Sample	EY [%]	Experimental EY range [%]
Fine	22.53	22.07–22.58
Optimal	20.44	20.43–20.87
Coarse	19.30	19.09–20.11

Fig. 3. Comparison between simulated and real EY values.

point in $\mathcal{R}^s$ are uniformly distributed. Moreover, as RBFs we choose the polyharmonic splines of exponent 3, that is $\varphi(r) = r^3$ and hence

$$\varphi_j(z) = |z - z_j|^3, \quad z_j \in \bar{\mathcal{Z}},$$
$$\varphi_j(r^s) = |r^s - r_j^s|^3, \quad r_j^s \in \bar{\mathcal{R}}^s, \ s = f, b.$$

We note that the polyharmonic splines possess desirable characteristics, such as their independence from the shape parameter. They also have certain limitations such as their accuracy compared to other RBFs. We tried other RBFs, such as the Gaussian, however, in our case, the polyharmonic splines were the most accurate. The maximum degree of the polynomial basis is $p = 3$. Moreover, we choose $N = 100$, $M^f = 4$, and $M^b = 40$; the numbers of time steps are $N_t = 800, 1000, 1500$, for coarse, optimal and fine granulometry, respectively. Thus $h_t \approx 10^{-2}$; the parameter α in (22) is 0.1. The relaxation parameters ω_l and ω_s, $s = f, b$, depend on the time step. In particular, $\omega_l = 0.9$ and $\omega_s = 0.75$, if $n \leq 15$; $\omega_l = \omega_s = 0.1$, $s = f, b$, otherwise. Finally, the tolerances are $tol_1 = 10^{-7}$ and $tol_2 = 10^{-6}$ and the maximum allowed iterations are $maxit_1 = maxit_2 = 500$.

Table 3 reports the parameters depending on the granulometry and computed from laboratory measurements. In particular, a^f and a^b come from the granulometry analyses of Fig. 2, ϕ^f is the volume percentage of fine particles with respect to the total solid fraction ϕ, q is the Darcy's flux and is inversely proportional to the granulometry. Finally, the percolation time τ is the mean of the ones in Table 2.

The EY is computed by Eq. (4), the integral is solved by the trapezoidal rule, and the liquid concentration c^l is obtained from the numerical results.

In Table 4, there are, for each granulometry, the mean EY obtained by the numerical simulations on all the samples used in the laboratory, and the EY range obtained from laboratory measurements. From this comparison, we can see that the computed average EY falls inside the laboratory range. The same results are shown in Fig. 3, where we have the EY along the y-axis and the granulometry along the x-axis; moreover the coloured squares represent the obtained numerical values, while the vertical bars are the laboratory ranges.

Fig. 4 shows the behaviour of c^l, for the optimal granulometry, as a function of the time t and the basket height z, by reporting on the vertical axes the mean of the liquid concentration computed at each considered sample. The other granulometries show similar behaviours. In particular, the liquid concentration at $z = L$, which is null at the
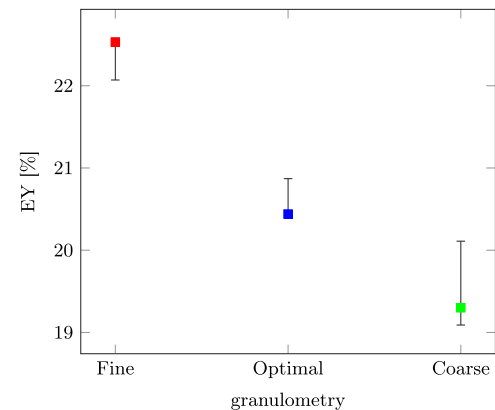
beginning $t = 0$, immediately increases, under the effect of dissolving substances, and decreases at the end of the extraction.

Figs. 5, 6(a) show the qualitative behaviour of the solid concentration c^s, $s = f, b$, at $z = L/2$, for the optimal granulometry. From Fig. 5 we can see that, in boulder particles, the external layer $r = a^b$ is more affected by dissolution than the core. From Fig. 6(a) we can see that, at the beginning of the extraction, the concentration of fine particles immediately decreases due to the dissolution, then for about the next five seconds, the concentration remains constant and finally decreases again, releasing the fines soluble material very quickly. This constant trend is very interesting, and it can be easily analysed with Fig. 6(b), which shows the liquid and fine solid concentration curves in blue and orange, respectively, over time and at $z = L/2$. In this figure it is plotted the fluid concentration c^f at $r = 0$ (the centre of the fine particle) however, analogous behaviour has been observed also at the boundary. When $c^f < c^l$, then $G^f = 0$, this means that the dissolution inside fines stops and c^f remains constant.

Finally, to give some numerical evidence of the convergence of the proposed solving strategy, in Table 5 we report the EY values for coarse granulometry under varying the discretisation parameter N. Also in this simulation we have that the computed EY is inside the range obtained in laboratory. We note that we do not vary the values of
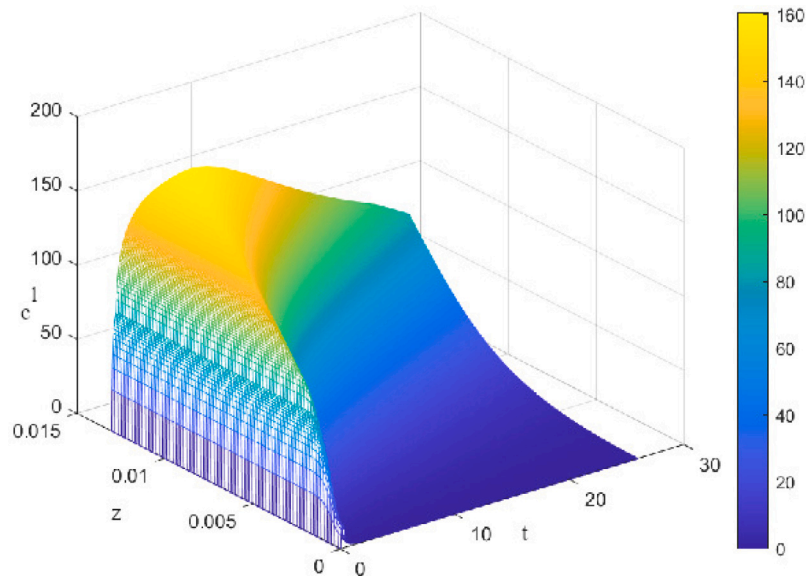
Fig. 4. Computed liquid concentration c^l with optimal granulometry.
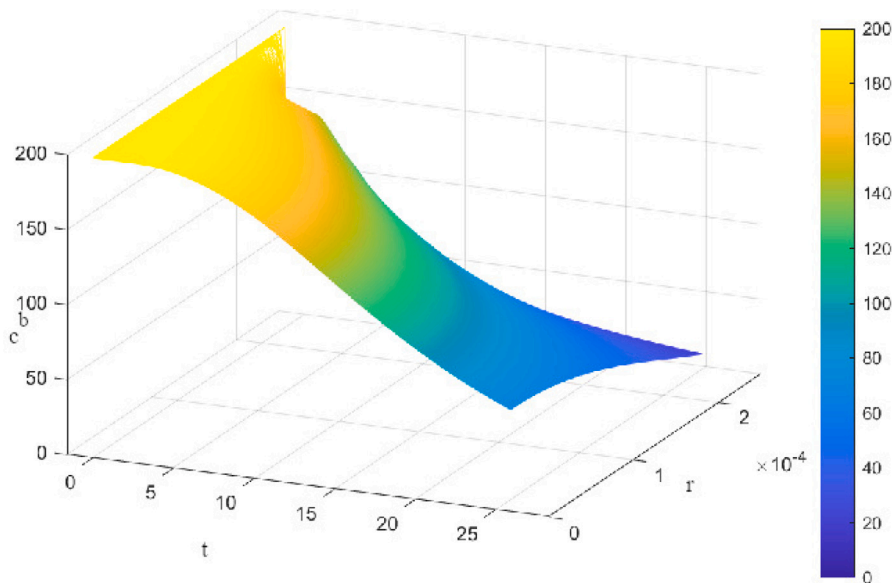

Fig. 5. Solid concentration of boulders c^b at $z = L/2$, during the simulated extraction with optimal granulometry.

Table 5
Comparison of the numerical EY value for coarse granulometry under varying discretisation parameter.

| N	EY [%]	Experimental EY range [%]
50	19.56	22.07–22.58
80	19.34	20.43–20.87
100	19.30	19.09–20.11

M^f and M^b since the EY is calculated only on the base of the liquid concentration $c^l(z, t)$.

5. Conclusions

In this work we proposed a simple tool for the coffee industry to evaluate the extraction efficiency. In particular, we considered the main processes occurring in the espresso coffee extraction, which, under some simplifying assumptions, is modelled through a one-dimensional ADR model. The proposed numerical scheme is based on a modified Crank–Nicolson method, where the spatial derivatives are approximated via RBFs while in [10] the finite differences have been used. The resulting system is solved with the proposed nested fixed-point iteration and the reliability of this strategy is experimentally assessed, in particular, the model is preliminarily validated by comparing the simulated and laboratory EY. From the results, we see that the model well simulates the dynamics of the extraction process in terms of extraction efficiency. In particular, by comparing the results with those obtained in [10], this new method gives a better approximation of the EY, even if it is more computationally expensive. Moreover, thanks to the use of a meshless technique, the proposed method can be easily generalised to higher dimensions, however, to get a better comparison, we should enlarge the extraction campaign.

Two future improvements have to be considered, to get a powerful simulation tool: the refinement of the numerical scheme, especially for treating the reactive parts, and the extension of the validation procedure with a larger set of laboratory experiments. Once these
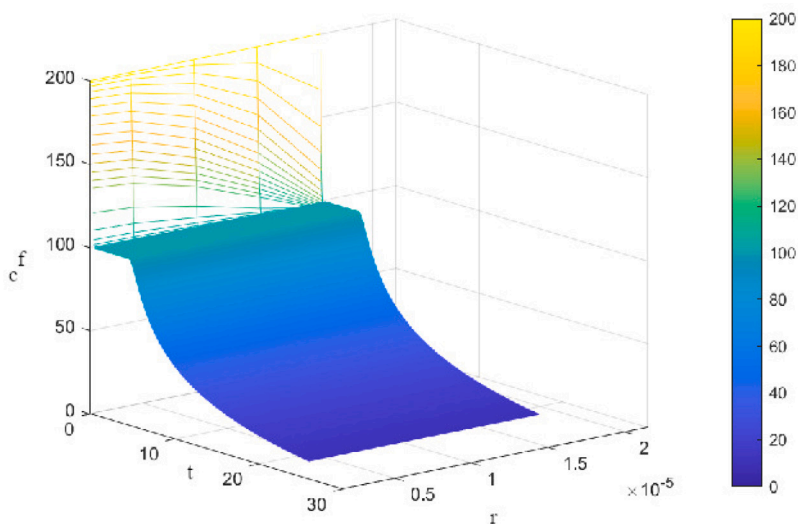
(a)
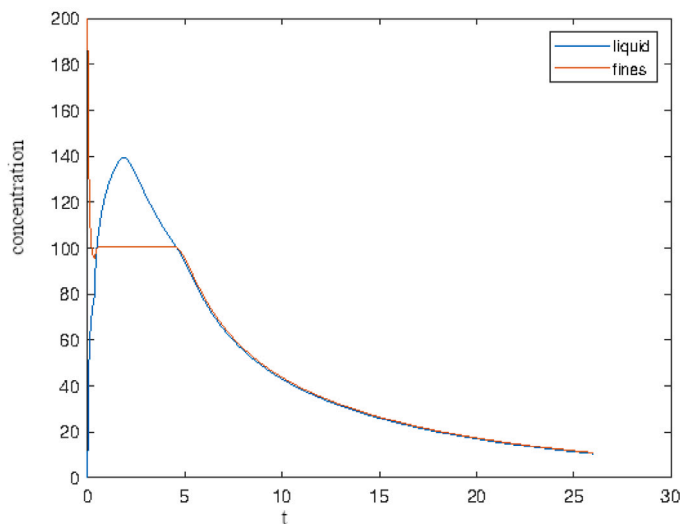
(b)

Fig. 6. (a) Solid concentration of fines c^f, and (b) Liquid (in blue) and solid concentration of fines at the centre of the particle (in orange) at $z = L/2$, during the simulated extractions with optimal granulometry. (For interpretation of the references to colour in this figure legend, the reader is referred to the web version of this article.)

refinements have been implemented, such a model allows the control of the percolation process concerning the total dissolved substances. Thus, this work paves the way for the study of challenging goals of the coffee industry, such as maximising the extraction efficiency while reducing the used coffee powder, and moving towards the sustainability aim.

Finally, we recall that the ADR equations are extensively used for modelling real-life phenomena, so the proposed discretisation scheme, although used to calculate the EY for coffee, has a great scope of applications in the engineering field. For this purpose, the great advantage of the proposed solving strategy is that it can be easily generalised to three-dimensional domains, thanks to the use of RBFs.

CRediT authorship contribution statement

Nadaniela Egidi: Writing – review & editing, Validation, Supervision, Methodology. **Josephin Giacomini:** Writing – review & editing, Validation, Supervision, Methodology. **Elisabeth Larsson:** Writing – review & editing, Supervision, Formal analysis, Conceptualization. **Alessia Perticarini:** Writing – original draft, Visualization, Validation, Software.

Declaration of competing interest

Data availability

The data are contained in the article.

Acknowledgements

N. Egidi et al.

Chaos, Solitons and Fractals: the interdisciplinary journal of Nonlinear Science, and Nonequilibrium and Complex Phenomena 188 (2024) 115625

"Research ITalian network on Approximation" and the UMI Group TAA "Approximation Theory and Applications".

References

[1] Illy A, Viani R. Espresso coffee: the science of quality. Academic Press; 2005.

[2] Angeloni G, Guerrini L, Masella P, Bellumori M, Daluiso S, Parenti A, et al. What kind of coffee do you drink? An investigation on effects of eight different extraction methods. Food Res Int 2019;116:1327–35.

[3] Gloess AN, Schönbächler B, Klopprogge B, Lucio D, Chatelain K, Bongartz A, et al. Comparison of nine common coffee extraction methods: instrumental and sensory analysis. Eur Food Res Technol 2013;236(4):607–27.

[4] Severini C, Derossi A, Ricci I, Caporizzi R, Fiore A, et al. Roasting conditions, grinding level and brewing method highly affect the healthy benefits of a coffee cup. Int J Clin Nutr Diet 2018;4(1):127.

[5] Andueza S, Maeztu L, Dean B, de Pena MP, Bello J, Cid C. Influence of water pressure on the final quality of arabica espresso coffee. Application of multivariate analysis. J Agricult Food Chem 2002;50(25):7426–31.

[6] Andueza S, De Peña MP, Cid C. Chemical and sensorial characteristics of espresso coffee as affected by grinding and torrefacto roast. J Agricult Food Chem 2003;51(24):7034–9.

[7] Salamanca CA, Fiol N, González C, Saez M, Villaescusa I. Extraction of espresso coffee by using gradient of temperature. Effect on physicochemical and sensorial characteristics of espresso. Food Chem 2017;214:622–30.

[8] Khamitova G, Angeloni S, Borsetta G, Xiao J, Maggi F, Sagratini G, et al. Optimization of espresso coffee extraction through variation of particle sizes, perforated disk height and filter basket aimed at lowering the amount of ground coffee used. Food Chem 2020;314:126220.

[9] Cameron MI, Morisco D, Hofstetter D, Uman E, Wilkinson J, Kennedy ZC, et al. Systematically improving espresso: insights from mathematical modeling and experiment. Matter 2020.

[10] Egidi N, Giacomini J, Maponi P, Perticarini A, Cognigni L, Fioretti L. An advection–diffusion–reaction model for coffee percolation. Comput Appl Math 2022;41(6):229.

[11] Giacomini J, Maponi P, Perticarini A. CMMSE: a reduced percolation model for espresso coffee. J Math Chem 2022;1–19.

[12] Moroney K, Lee W, O'Brien S, Suijver F, Marra J, et al. Modelling of coffee extraction during brewing using multiscale methods: An experimentally validated model. Chem Eng Sci 2015;137:216–34.

[13] Giacomini J, Khamitova G, Maponi P, Vittori S, Fioretti L. Water flow and transport in porous media for in-silico espresso coffee. Int J Multiph Flow 2020;103252.

[14] Angeloni S, Giacomini J, Maponi P, Perticarini A, Vittori S, Cognigni L, et al. Computer percolation models for espresso coffee: State of the art, results and future perspectives. Appl Sci 2023;13(4):2688.

[15] Moroney KM, O'Connell K, Meikle-Janney P, O'Brien SBG, Walker GM, Lee WT. Analysing extraction uniformity from porous coffee beds using mathematical modelling and computational fluid dynamics approaches. PLoS One 2019;14(7).

[16] Moroney KM, Lee WT, O'Brien S, Suijver F, Marra J. Asymptotic analysis of the dominant mechanisms in the coffee extraction process. SIAM J Appl Math 2016;76(6):2196–217.

[17] Liu H, Lü S. A high-order numerical scheme for solving nonlinear time fractional reaction-diffusion equations with initial singularity. Appl Numer Math 2021.

[18] Clairambault J. Reaction-diffusion-advection equation. In: Dubitzky W, Wolkenhauer O, Cho K-H, Yokota H, editors. Encyclopedia of systems biology. New York, NY: Springer New York; 2013, p. 1817.

[19] Rubio A, Zalts A, El Hasi C. Numerical solution of the advection–reaction–diffusion equation at different scales. Environ Model Softw 2008;23(1):90–5.

[20] Chen-Charpentier BM, Kojouharov HV. An unconditionally positivity preserving scheme for advection–diffusion reaction equations. Math Comput Model 2013;57(9–10):2177–85.

[21] Shahid N, Ahmed N, Baleanu D, Alshomrani AS, Iqbal MS, Rehman MA-u, et al. Novel numerical analysis for nonlinear advection–reaction–diffusion systems. Open Phys 2020;18(1):112–25.

[22] Sarra SA. A local radial basis function method for advection–diffusion–reaction equations on complexly shaped domains. Appl Math Comput 2012;218(19):9853–65.

[23] Mirzaee F, Rezaei S, Samadyar N. Numerical solution of two-dimensional stochastic time-fractional Sine–Gordon equation on non-rectangular domains using finite difference and meshfree methods. Eng Anal Bound Elem 2021;127:53–63.

[24] Mirzaee F, Rezaei S, Samadyar N. Solution of time-fractional stochastic nonlinear sine-Gordon equation via finite difference and meshfree techniques. Math Methods Appl Sci 2022;45(7):3426–38.

[25] Naderi M. Surface area: Brunauer–Emmett–Teller (BET). In: Progress in filtration and separation. Elsevier; 2015, p. 585–608.

[26] Moroney KM, Lee WT, O'Brien SB, Suijver F, Marra J. Coffee extraction kinetics in a well mixed system. J Math Ind 2016;7(1):1–19.

[27] Schoenberg IJ. Metric spaces and completely monotone functions. Ann of Math 1938;811–41.

[28] Fasshauer GE. Meshfree approximation methods with MATLAB, vol. 6. World Scientific; 2007.

[29] Micchelli CA. Interpolation of scattered data: Distance matrices and conditionally positive definite functions. Constr Approx 1986;11–22.

[30] Va388 black eagle. 2021, https://www.victoriaarduino.com/black-eagle/ Visited on 2021.

[31] Mythos 1. 2021, https://www.victoriaarduino.com/mythos-1/ Visited on 2021.

[32] Puq press tamper. 2021, https://www.puqpress.com/products/puq-m-line/puqpress-m2-for-mythos/ Visited on 2021.

[33] Mastersizer: malvern panalytical. 2021, https://www.malvernpanalytical.com/en/products/product-range/mastersizer-range Visited on 2021.